Ti–6Al–4V complex shape production by spark plasma sintering with ceramic–metal sacrificial powder and interface 3D printing

Joseph Le Cloarec, Sylvain Marinel, Claude Estournès, Moukrane Dehmas, Charles Manière

To cite this version:

Joseph Le Cloarec, Sylvain Marinel, Claude Estournès, Moukrane Dehmas, Charles Manière. Ti–6Al–4V complex shape production by spark plasma sintering with ceramic–metal sacrificial powder and interface 3D printing. Progress in Additive Manufacturing, 2024, ⟨10.1007/s40964-024-00803-w⟩. ⟨hal-04738221⟩

HAL Id: hal-04738221
https://normandie-univ.hal.science/hal-04738221v1

Submitted on 15 Oct 2024

Ti-6Al-4V complex shape production by spark plasma sintering with ceramic-metal sacrificial powder and interface 3D printing

Joseph Le Cloarec[1,2]*, Sylvain Marinel[1], Claude Estournès[2], Moukrane Dehmas[3], Charles Manière[1]*.

1. CRISMAT, Normandie Univ, ENSICAEN, UNICAEN, CNRS, 14000, Caen, France
2. CIRIMAT, Université Toulouse 3 Paul Sabatier, Toulouse INP, CNRS, Université de Toulouse, 118 Route de Narbonne, 31062 Toulouse cedex 9 - France
3. CIRIMAT, Toulouse INP, Université Toulouse 3 Paul Sabatier, CNRS, Université de Toulouse, 4 allée Emile Monso - BP44362, 31030 Toulouse cedex 4 – France

* Corresponding authors:
E-mail address: joseph.le-cloarec@ensicaen.fr; charles.maniere@ensicaen.fr

Keywords

Spark Plasma Sintering; Complex Shape; 3D printing; sintering simulation; Ti-6Al-4V titanium alloy.

Abstract:

The production by Spark Plasma Sintering (SPS) of parts with high complex shapes is difficult due to the die pressing which imposes adapting the die and punches in a too complex and fragile configurations. To overcome this problem, a patented approach called “DEFORMINT”, allows the production of fully dense complex shape parts by coupling 3D printing and SPS technologies. Thus, an assembly of two-powder beds, one constitutive of the desired complex shape part while the second one is sacrificial, separated by a 3D printed interface sinter simultaneously. The easiest way to avoid any shape distortions of the part is to use the same powder for both the complex shape and the sacrificial parts. However, for high added value parts, the cost of the materials and the high quantity of sacrificial material needed in this method reduces its inherent economic interest. To circumvent this issue particularly for Ti-6Al-4V, a low-cost ceramic-metal powder mixture that mimics its sintering was identified and tested in this study. SPS experiments were used to determine a densification model of this sacrificial powder and to predict the densification distortions of two shapes: a thick cone and a thin and complex turbine blade. The simulated and experimental distortions were compared and showed a good correlation with the predicted shape distortions. Microstructural analysis revealed a high hardness globular microstructure and a skin effect in the contact with the interface. This process provides valuable outcomes for prototyping, as well as for complex structural parts with thick geometries that are less sensitive to the skin effect (in contrast to SLM, which is more effective for thin shapes). It can create significant opportunities in the space, aeronautics, and engine industries.

Graphical Abstract:

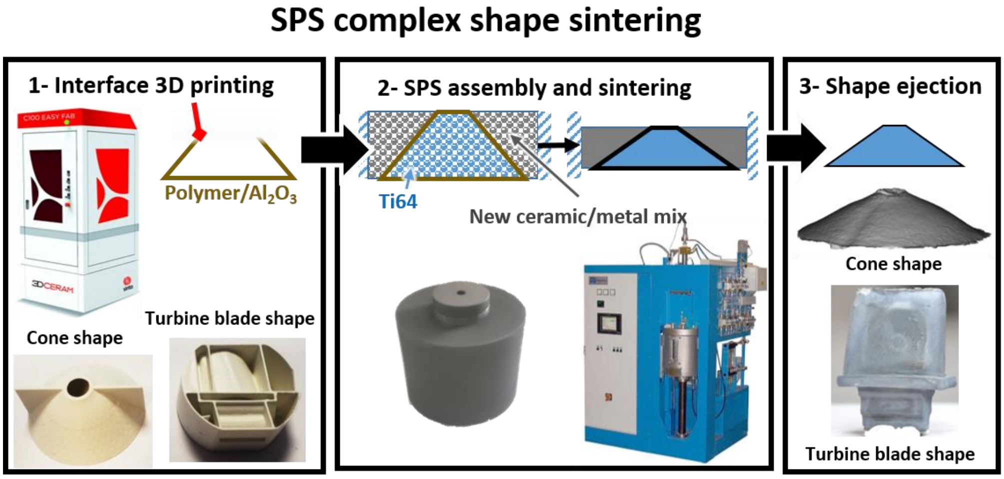

Nomenclature and abbreviations

θ Porosity

$\dot{\theta}$ Porosity elimination rate (s^{-1})

$\underline{\sigma}$ Stress tensor ($N.m^{-2}$)

σ_{eq} Equivalent stress ($N.m^{-2}$)

$\underline{\dot{\varepsilon}}$ Strain rate tensor (s^{-1})

n Creep law stress exponent

A_0 Deformability pre-exponential factor ($Ks^{-1}Pa^{-n}$)

Q Deformability activation energy ($J.mol^{-1}$)

T Temperature (K)

φ Shear modulus

ψ Bulk modulus

$\dot{\varepsilon}_z$ Axial strain rate tensor component (s^{-1})

σ_z Axial stress tensor component ($N.m^{-2}$)

θ_{cf} Critical final porosity

SPS Spark Plasma Sintering

SLM Selective Laser Melting

1. Introduction

In the spark plasma sintering (SPS) process, the die pressing configuration makes the fabrication of 3D complex shapes very challenging [1–3]. Multiple-punches configuration can be used [4], however, unlike powder metallurgy [5], where gears, in particular, can be mass-produced, achieving full densification of parts by SPS with differential punch motion is very difficult, if not impossible. Alternatively, sacrificial powder can be used to control the motion of a limited number of punches [6] but this approach is limited to relatively flat shapes with a restricted number of thickness variations (2 or 3 at most), like gears. This sacrificial powder can, in principle, mimic the powder metallurgy gear fabrication process, but the use of fragile graphite tool limits the possible shape complexity. For highly complex shapes like turbine blades or any 3D shapes with continuous thickness variations, another approach can be used. This method uses deformable internal inert interfaces [7] and is called "DEFORMINT". One of the most promising aspects of this approach is the possibility to use a high-resolution 3D printing process to generate a thin interface, consisting of a ceramic charge bound by a polymer, which acts as a sub-mold in the SPS die [8]. During the SPS thermal cycle performed under vacuum, the polymer compound partially degrades into graphite creating an inert graphite/ceramic separation interface that eases the post SPS ejection of the 3D complex shape [9]. The use of vat photopolymerization is particularly suitable for this approach, as ceramic/polymer interfaces of very fine complex shapes can be obtained with a wall thickness down to 0.2 mm and a high resolution of 10 to 50 µm [10–14]. There are two main challenges for this interface method coupling 3D printing with SPS. The first is the post-SPS ejection of the complex shape, where the 3D printed interface should not adhere to the shape during SPS. The second is the interface, which can experience distortions due to its different sintering behavior compared to the constituent powder of the part. This effect can be minimized by the use of thin interfaces but a minimal thickness is required to eject the shape after SPS. In general, the assembly is made of a metallic powder for the desired part, the 3D printed interface materials and the sacrificial powder. The latter is used to surround the shape and homogenize the pressure during the SPS cycle, therefore the complex shape compact sinters with a homogeneous and predictable displacement field. Another method, called “pseudo-isostatic”, uses recyclable granules as pressing medium [15]. However, the strong inherent hot compaction behavior between the sintered powder and the granules causes severe distortions in the shapes unless the part is highly pre-sintered [16, 17]. For this reason, the “DEFORMINT” method often uses the same powder in the complex shape zone and in the sacrificial zone. This ensures precise control of the shape evolution during SPS, where the only sources of distortion are the thin interface deformation and the powder/die wall friction, both of which are minimal [18]. If these distortions are minimal, the SPS initial shapes can be easily predicted by a simple uniaxial scale factor that is the ratio of the final relative density (D_{final}) of the part to the initial relative density of the powder ($D_{initial}$) [7].

However, the sacrificial powder (which is needed to produce complex shapes) represents a significant material loss. It represents the same level of loss as machining does on sintered regular shapes. If the cost of the powder used for the complex shape is high, it significantly deteriorates the economic interest of the method. By comparison, the SLM process practically incurs no materials losses but the critical thickness of the shape is limited to about 10 mm or less due to the thermal stress involved. In this context, the “DEFORMINT” approach (based on SPS) is more oriented to the production of structural thick shapes [19, 20].

In this study, a Ti-6Al-4V alloy powder is used for the complex shape. The main objective is to identify and evaluate a “low-cost” and “environment-friendly” powder mixture to be used as sacrificial powder in the DEFORMINT process, which mimics the sintering behavior of Ti-6Al-4V in SPS conditions. In contrast to our previous work [21], where the same Ti-6Al-4V powder was used as a sacrificial material, this low-cost approach aims to address the economic issues associated with the “DEFORMINT” method, which have not yet been resolved. The sintering difference between the Ti-6Al-4V and the sacrificial powder mixture may generate distortions in the sample. Consequently, the sintering behavior of the sacrificial powder mixture will be first modeled by finite element method (FEM) from the SPS densification curves. A method combining a multiple pressure step SPS method [22] and a model linearization [23, 24] is used to identify the powder densification parameters and the sintering model stress sensitivity. A similar simulation approach has been used to model SPS of complex shapes using graphite sacrificial powder [25, 26]. The Ti-6Al-4V powder and interface SPS behavior have been identified in a previous article [21]. The sintering model of the sacrificial powder mixture identified, the co-sintering of the three materials assembly Ti-6Al-4V/interface/sacrificial powders is simulated by FEM to explain the distortions observed experimentally and to find solutions to minimize or avoid them. This study analyzes two types of complex shapes: a conical shape to reveal the magnitude of the powders/interface distortions by sintering dissimilarities and a turbine blade to test the method on a thin highly complex shape.

2. Experiment and method

2.1. SPS sintering model and parameter determination method

The finite element model obeys the continuum theory of sintering [27] where the material behavior is the following:

$$\underline{\sigma} = \frac{1}{A{\sigma_{eq}}^{n-1}}\left(\varphi\underline{\dot{\varepsilon}} + \left(\psi - \frac{1}{3}\varphi\right)\dot{e}\mathbb{1}\right) \tag{1}$$

For SPS case, the following analytical equation [28] is used:

$$|\dot{\varepsilon}_z| = \left|\frac{\dot{\theta}}{(1-\theta)}\right| = A_0\frac{\exp(\frac{-Q}{RT})}{T}\left(\psi + \frac{2}{3}\varphi\right)^{\frac{-n-1}{2}}(1-\theta)^{\frac{1-n}{2}}|\sigma_z|^n \tag{2}$$

The identification of the sintering parameters (n, A_0 and Q) is performed in two stages. The stress exponent (*n*) is determined using isothermal SPS tests with the stepwise pressure method [22, 24, 29]. In this method, the model stress exponent n is determined by the ratio of the porosity elimination rates before and after the pressure “jump” and the stress ratio. See the following equation:

$$n = \frac{ln\left(\frac{\dot{\theta}_1}{\dot{\theta}_2}\right)}{ln\left(\frac{\sigma_1}{\sigma_2}\right)} \tag{5}$$

Once the “*n*” is determined, the temperature dependent parameters (*A_0, Q*) are determined by a linear regression using a heating ramp SPS test and the following equation [30]:

$$Y = ln\left(\frac{T|\dot{\theta}|}{\left(\psi+\frac{2}{3}\varphi\right)^{\frac{-n-1}{2}}(1-\theta)^{\frac{3-n}{2}}|\sigma_z|^n}\right) = ln(A_0) - \frac{Q}{RT} \tag{6}$$

With the modified Skorohod’s [31] theoretical moduli:

$$\psi = \left(\frac{2}{3}\right)\frac{(1-\theta)^3}{(\theta-\theta_{cf})} \tag{3}$$

$$\varphi = (1-\theta)^2 \tag{4}$$

In the latter, θ_{cf} corresponds to the final stage macro-porosity that is not easily removed. This linear regression equation is applied on the experimental data and is used to determine A_0 and

Q parameters. By plotting Y as a function of 1/RT, the sintering activation energy Q is given by the slope of the curve and A_0 by the exponent of the curve's origin.

The resulting modeling parameters are first tested analytically using the software GNU Octave 5.1.0. If these parameters reproduce well the experimental data points, they will be incorporated in COMSOL multiphysics 5.0 finite element code.

2.2. Complex shape production method combining 3D printing and SPS

The complex shape sintering method (DEFORMINT) has been detailed in a previous work [21]. As mentioned previously, this method consists of simultaneously sintering an assembly of a working powder bed and a sacrificial powder bed separated by an interface. As illustrated in Figure 1.a, the interface is 3D printed as an elongated shape of the final part made by vat photopolymerization. Then, the interface is placed in the SPS tooling and internally filled with working powder, Ti-6Al-4V alloy here. The sacrificial zones are filled with a low-cost powder mixture that sinters in a similar way to the Ti-6Al-4V powder. To facilitate the loading of this powder mixture into the printed interface, it is formulated as a thick aqueous slurry. The entire assembly forms a cylinder that can be easily sintered using SPS. The composition of the sacrificial media is currently confidential, however, it consists of a mixture of ceramic and metallic powders designed to mimic the sintering behavior of the Ti-6Al-4V powder under SPS conditions. During SPS densification, the interface made of polymer/ceramic interface partially degrades in a graphite/ceramic separation interface. This was initially established in a patent [8] and subsequently used to produce turbine blades shapes, as described in our previous article [21]. It remains a thin powdered interface, which follows the shrinkage of the main powders assembly. After sintering, since the interface remains in a powder state, the final part can be easily ejected from the sacrificial parts.

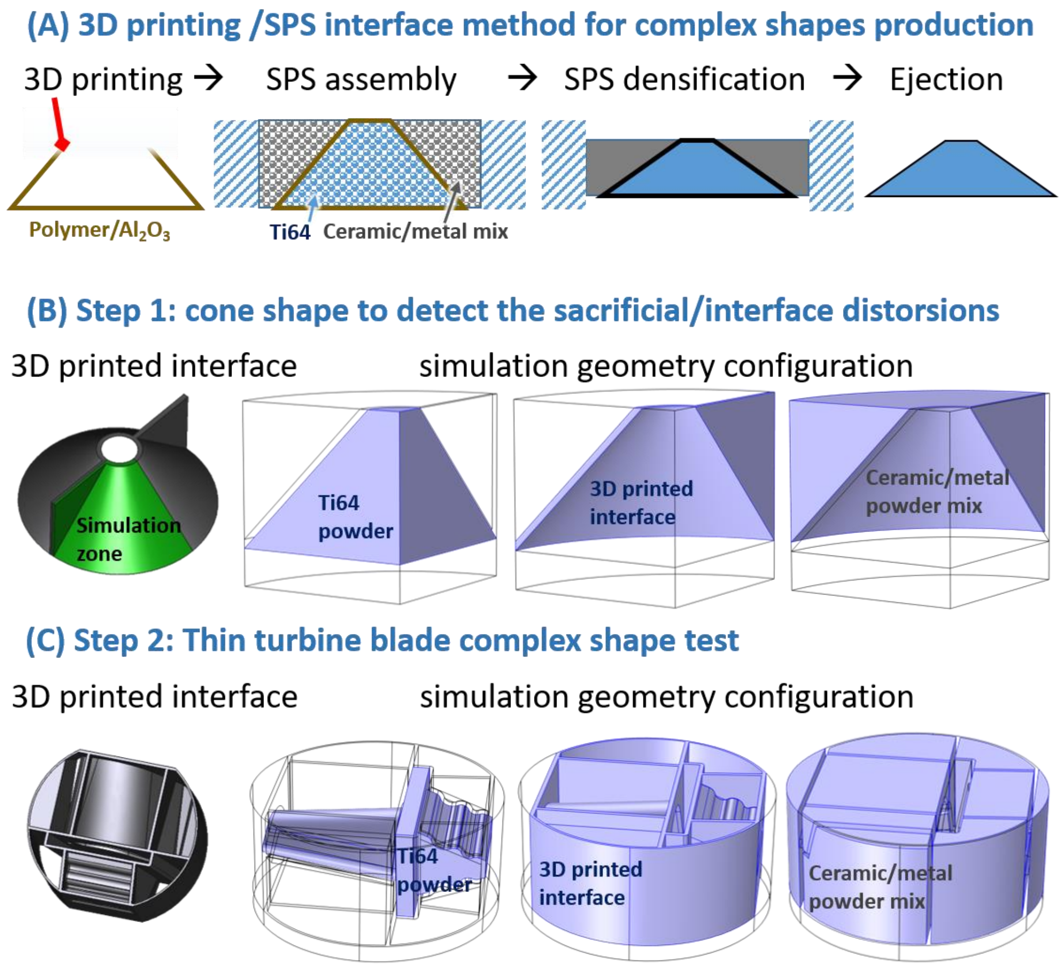

Figure 1 : (a) Steps of complex shape method (DEFORMINT), which couple 3D printing and SPS. (b) Cone interface and simulation geometry configuration of cone sintering. (c) Turbine blade interface and simulation geometry configuration of turbine blade sintering.

To ensure a homogeneous stress field during sintering, the sacrificial powder must shrink simultaneously with the main material. If the stress field is heterogeneous during sintering, shape defects can appear on the final parts. It is also necessary that the total shrinkage of the sacrificial powder is greater than or equal to the total shrinkage of the working powder to ensure full densification of the latter. To test the ceramic-metal sacrificial powder mixture, a simple cone shape is sintered. The sintering simulation of this assembly is also performed to predict possible shape or densification defects of the part. In Figure 1.b, the 3D object of the conic interface is reported. This cone test is very important because it helps detect sintering defects caused by differences in the sintering behavior of the shape and sacrificial powders, as well as deformation at the interface itself. This test is first used to evaluate the three materials co-sintering compatibility in terms of deformation. The green part corresponds to the simulation geometrical domain that can be reduced to a quarter thanks to the axis symmetry of the shape geometry. On the right side, the geometrical configuration of the simulations is reported with the three parts of the assembly, the Ti-6Al-4V powder bed inside the conic interface and the ceramic-metal powder bed outside the conic interface. After the cone test, the same sintering experiment and simulation are performed on a more complex shape, such as a turbine blade. In Figure 1.c, the turbine interface and the geometrical configuration of the simulation are presented. For the latter, the geometry does not allow geometrical simplification, so the full 3D geometry was then modelled. For both complex shapes, the microstructure and relative density are controlled.

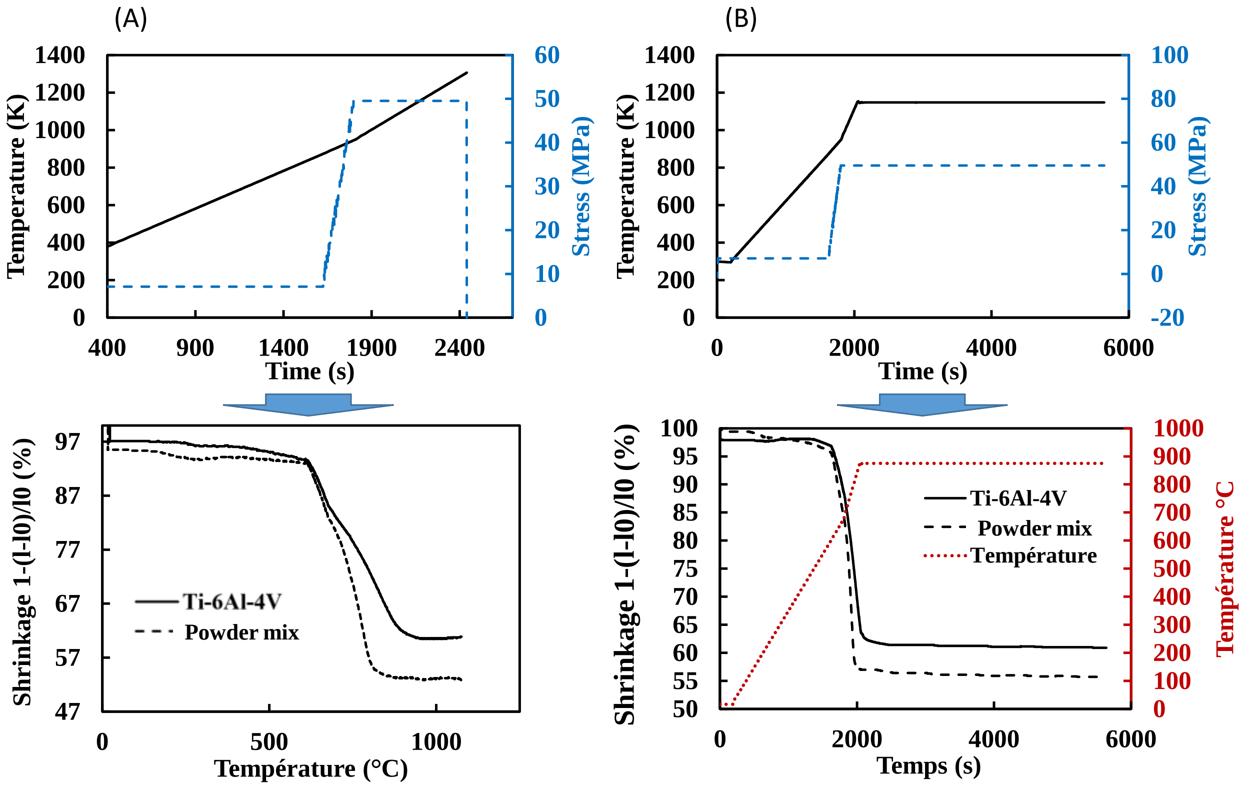

Figure 2: (a) SPS cycle experienced by the cone assembly. (b) SPS cycle experienced by the turbine blade assembly, in the lower part, the sintering shrinkage of the reference Ti-6Al-4V powder and the ceramic/metal powder mix is presented. This demonstrates the excellent correspondence between the sintering shrinkages of the powder mix and the Ti-6Al-4V powder, as the mix sinters at a similar temperature and achieves slightly higher densification, which facilitates the complete densification of the Ti-6Al-4V part.

Figure 2.a shows the thermal and pressure cycles experienced by the cone assembly. The temperature is increased at a rate of 25 K/min from room temperature up to 900 K, to ensure gradual degradation of the interface. Then, the temperature is increased with a heating rate of 50 K/min up to 1300 K. Up to 900 K, the applied stress is only of about 7 MPa (the minimum applicable) to allow possible gaseous by-products of the degradation of the polymer to be eliminated, this pressure is then increased up to 50 MPa in one minute once 900 K is reached. This pressure remains constant until the final temperature is reached. Once the set temperature of 1300 K is reached, the SPS is stopped and the assembly is freely cooled under the minimal pressure of 7 MPa. In Figure 2.b, the cycle experienced by the turbine blade assembly is reported. It is the same as for the cone assembly, except that the turbine blade assembly temperature reaches 1150 K instead of 1300 K, and is maintained at this temperature for 1 h. Since the turbine blade is thinner and more brittle than the cone, the maximum cycle temperature is reduced to limit the thermal contraction differences between the sacrificial powder and the Ti-6Al-4V alloy. These thermal contractions of the assembly during the cooling lead to significant residual stresses in the turbine blade. These residual stresses can lead to the turbine blade breakage during the cooling or its ejection from the SPS die. The temperature and pressure are maintained for 1 h to allow the Ti-6Al-4V alloy to reach the maximum relative density. Additionally, the assembly is cooled without pressure to minimize thermal contraction differences and residual stresses.

Figure 2 shows the SPS shrinkage for both the reference Ti-6Al-4V powder and the sacrificial “powder mix” for each cycle. This comparison demonstrates that the sacrificial “powder mix” closely mimics the sintering behavior of the Ti-6Al-4V, with similar sintering temperatures and shrinkage amplitudes. However, the sacrificial ‘powder mix’ exhibits a slightly higher shrinkage amplitude. This is a crucial safety feature, as a lower sintering amplitude in the sacrificial powder compared to the part could result in incomplete densification of complex shapes.

2.3. Instrumentation

SPS experiments are realized on an SPS apparatus “FCT HPD25” with graphite grade Mersen 2333 dies, punches and spacers. The Ti-6Al-4V grade 5 powder (35 µm in average diameter) is supplied by AP&C. The powder properties are detailed in a previous work [21]. In all SPS experiments, a boron nitride is deposited on the graphite paper located between the punchers and the assembly to insulate the powder (electrically) and prevent overheating. For the stress exponent “n” determination of the ceramic-metal powder mixture, an isothermal SPS experiment at 1020 K in a 15 mm inner diameter die with two pressures “jump” has been performed, from 28 MPa to 56 MPa and 56 MPa to 85 MPa. For A_0 and Q determination by regression, a 50 K/min heating rate experiment to 1300 K was used at a constant pressure of 50 MPa. The simulation parameters A_0, Q and n for Ti-6Al-4V powder has already been determined in previous work [21].

To reveal microstructure, the complex shapes have been cut and their cross-sections were etched for 2 s with a solution of chloric acid, fluoric acid and nitric acid: 30 % HCl; 10 % HF; 10 % HNO_3; 50 % H_2O. Vickers hardness has been measured with a “MICROPRESI MATSUTAWA MMTx7” under a loading of 0.5 kgF.

The complex 0.5 mm thick interfaces were printed with a professional ceramic vat photopolymerization printer, the ceramaker 100 from 3DCERAM SINTO® and the alumina resin “3DMix AL-E02” was used. The printing conditions were set as follows: a laser power of 50 mW, a lasing speed of 10000 mm/s, and a layer height of 50 µm.

The Ti-6Al-4V sintered cone part was scanned with an EinScan-SP 3D scanner with an accuracy of 30 µm.

3. Results and discussions

In this section, the identification of the sintering parameters of the sacrificial powder mixture is first presented. Then, the experimental and simulated cone and turbine blade shapes are compared and characterized.

3.1. Stress exponent n determination

In Figure 3, the true strain and applied stress of the "stepwise" test of the ceramic-metal powder mixture are reported. The measurements of stress and porosity rate elimination before and after each pressure step allow to determine the stress exponent "*n*". The red parts on the strain curve correspond to the parts used to calculate the porosity elimination rates. The n average value determined with this experiment is 1.65. A n value of 1 indicates dominant diffusional mechanism while n=2 indicates grain boundary sliding (GBS) [32]. This value of 1.65 seems to indicate grain boundary sliding but, considering the presence of a ceramic-metal powder mix, a specific and complex combination of mechanisms cannot be excluded. Nevertheless, this value, ranging between 1 and 2, is common in SPS [29, 33, 34] and can be considered an experimental value.

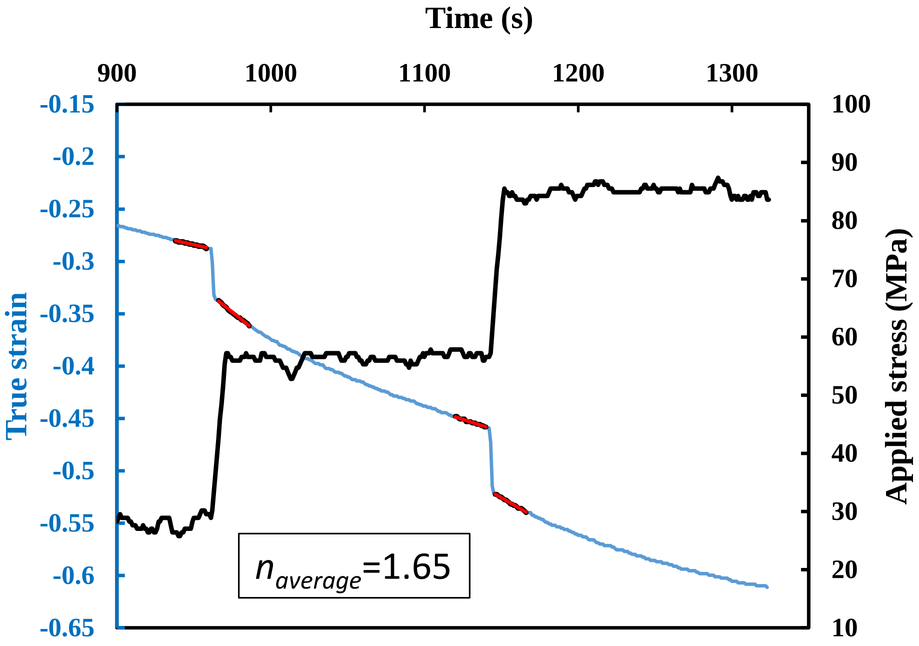

Figure 3: True strain and applied pressure during the identification test of the ceramic-metal sacrificial powder.

3.2. Temperature dependent parameter identification (A_0 and Q)

In Figure 4.a, the temperature and relative density of the ceramic-metal powder mixture during the SPS experiment are reported. From these data and by linearizing the analytic equation of SPS, the A_0 and Q values have been determined. In Figure 4.b, the linear regression is shown, revealing an A_0 value of 2739 K/(s Pa^n) and an activation energy Q of 308 kJ/mol. As this composition is a ceramic /metal powder mix, the previous values are effective values for the mixture.

With n, A_0 and Q identified, the SPS sintering model for the sacrificial powder is complete. In Figure 4.c, the experimental densification curve and the results of the sintering simulation are reported. With a θ_{cf} calibrated at 0.007 to adjust the final stage sintering values, the simulation data show very good agreement with the experimental results. This verification confirms the efficiency of the model to predict the sacrificial powder densification by SPS.

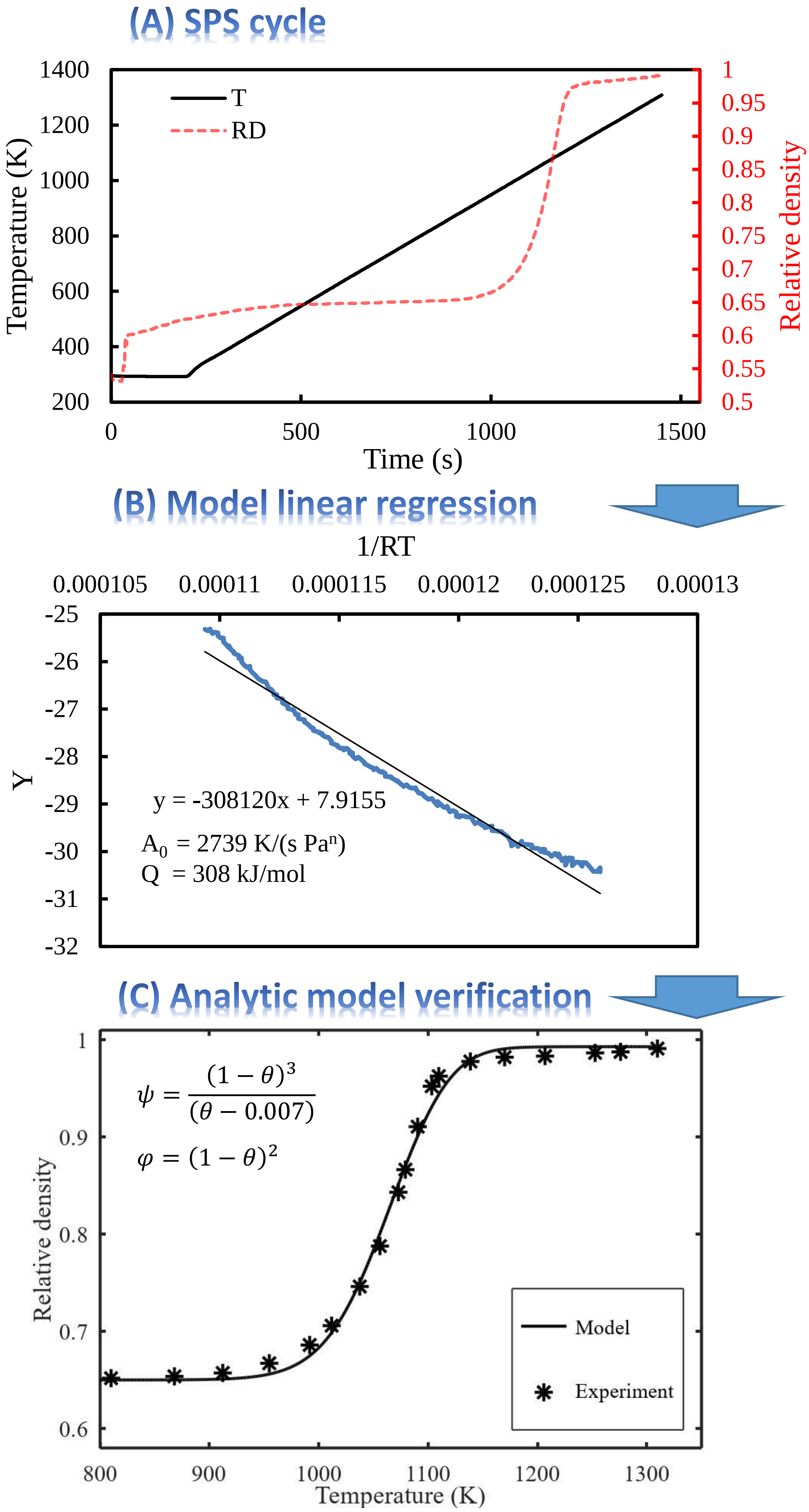

Figure 4: (a) Experimental data from SPS of the ceramic-metal sacrificial powder mix. (b) Linear regression of the analytic equation of SPS based on heating rate experimental sintering data of the ceramic-metal sacrificial powder mix. (c) Experimental and simulated sintering cures comparison.

In Figure 5, the FEM simulated densification curves (i.e. average relative density) of the Ti-6Al-4V alloy and the sacrificial powder are reported for the cone and turbine blade. As neither of the two powders sinter below 900 K, the simulations display only the end of the SPS cycle. For the cone assembly, Figure 5.a, heating with a rate of 50 K/min from 900 K up to 1350 K is applied. For the turbine blade assembly, Figure 5.b, the temperature is increased with a rate of 50 K/min from 900 K to 1150 K, and then the temperature is maintained for 1 h. Although these powders sinter over the same temperature and shrinkage ranges, there is a density gap between the Ti-6Al-4V alloy and the sacrificial powder, which densifies at relatively lower temperatures, although its densification rate decreases at the end of the cycle. This difference does not affect the sintering of the cone, which has thick shape. However, the thin turbine blade, that was initially sintered using the same cycle (like for the cone), shows cracks and a brittle behavior (see photo in Figure 5.a). For this reason, the new cycle with a dwell temperature of 1150 K and a dwell time of 1 h was applied to reduce the magnitude of the gap between the densification curves (see Figure 5.b) while also minimizing the thermal contraction stresses during cooling. With this cycle, the turbine blade was successfully produced without cracks.

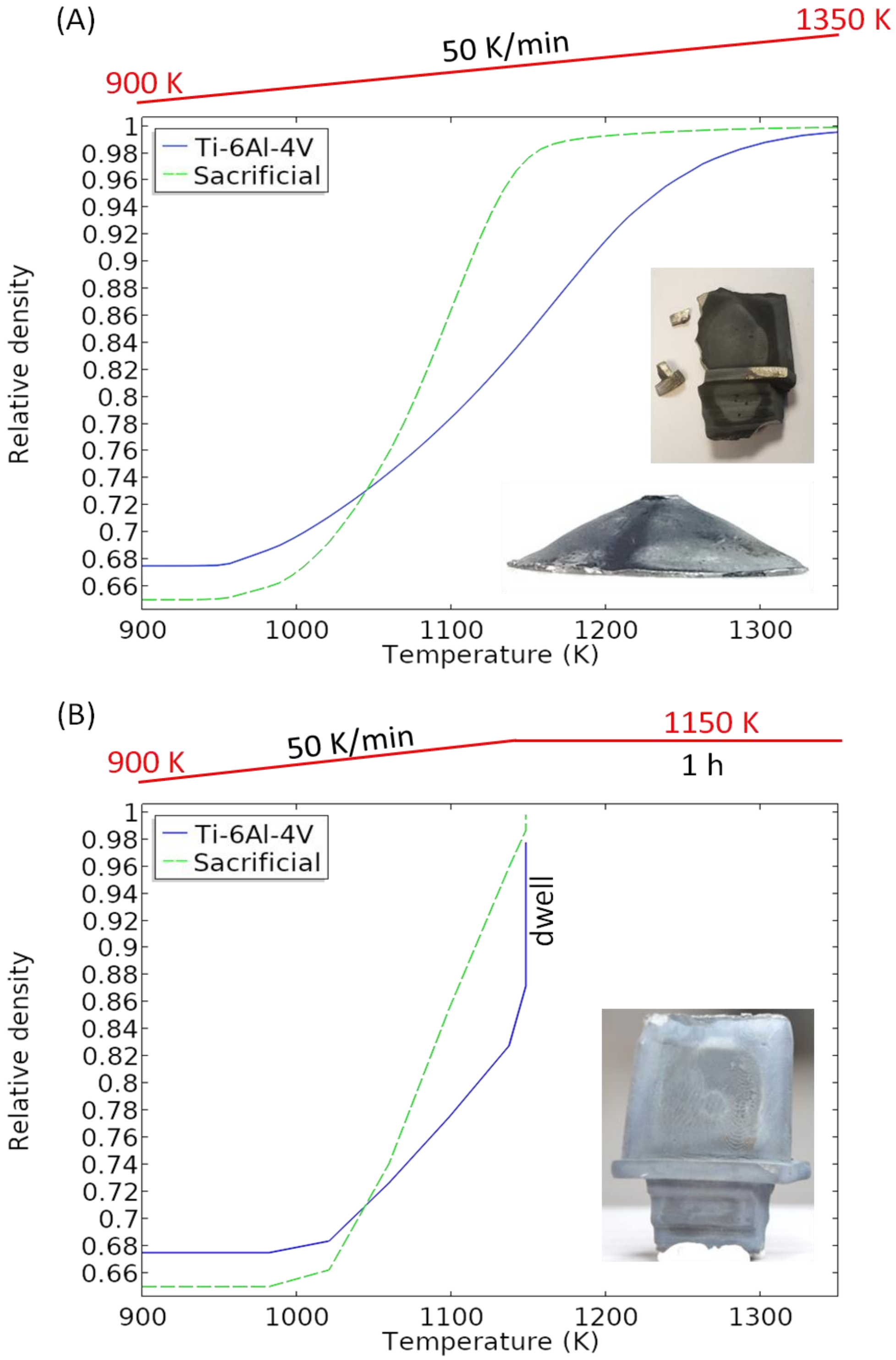

Figure 5: FEM co-sintering curves of the powders by SPS for the (a) cone and (b) turbine blade cycles

3.3. Cone SPS case: simulation and experimental comparison

The simulation of the evolution of the cone powder assembly densification is reported Figure 6.a,. Even if the sacrificial powder sinters at a slightly lower temperature than the Ti-6Al-4V, the cone reaches a high relative density at the end of the simulation. During the sintering, two shape defects appear. A depression forms beneath the thin wall of the interface, and the edge of the cone is rounded. The Figure 6.b shows the simulated cone shape and a 3D scan of experimental cone sample. The experimental shape evidences these distortions predicted by the simulation. Those defects are not due to the sacrificial powder behavior but to the interface that behaves in a slighter rigid way. These defects have been detected in a previous work with Ti-6Al-4V as sacrificial powder [21]. The density measured by Archimede's method of the experimental cone is 98 %. Its microstructure is reported in Figure 6.c. The microstructure mainly consists of α phase in globular morphology, with some α lamellae surrounded by β matrix. Based on this observation, it is proposed that the microstructure remains α + β two-phase despite the temperature of 1350 K, which is higher than the β transus temperature at thermodynamic equilibrium for the nominal composition. Additionally, the effective material stress is sufficient to fragment a significant amount of the existing lamellae at 1350 K [35]. This stress, which fragments the lamellae, is probably the result of the combination of the applied stress (50 MPa) and the thermal expansion coefficient disparities between sacrificial material and metallic parts. In addition, cooling is sufficiently slow to lead to the growth of existing globular α phase, as no disparity in size is observed. The presence of α phase at 1350 K can be explained by oxygen contamination, which stabilizes the α phase at higher temperatures. In addition, the increase in the oxygen content strengthens (solid solution hardening) the α phase [36], which is confirmed by a slightly higher hardness ($HV_{0.5}$ 439 ± 5) than reported in the scientific community [20, 37, 38]. On the edges of the cone, a 20 µm skin with a significant change in the size and shape of α phase is noticeable due to carbon contamination; this phenomenon has already been detailed in a previous work [21]. To confirm this carbon contamination, an EDSmap on the edge is shown in Figure 6.c. This clearly shows that these intergranular phases are rich in carbon.

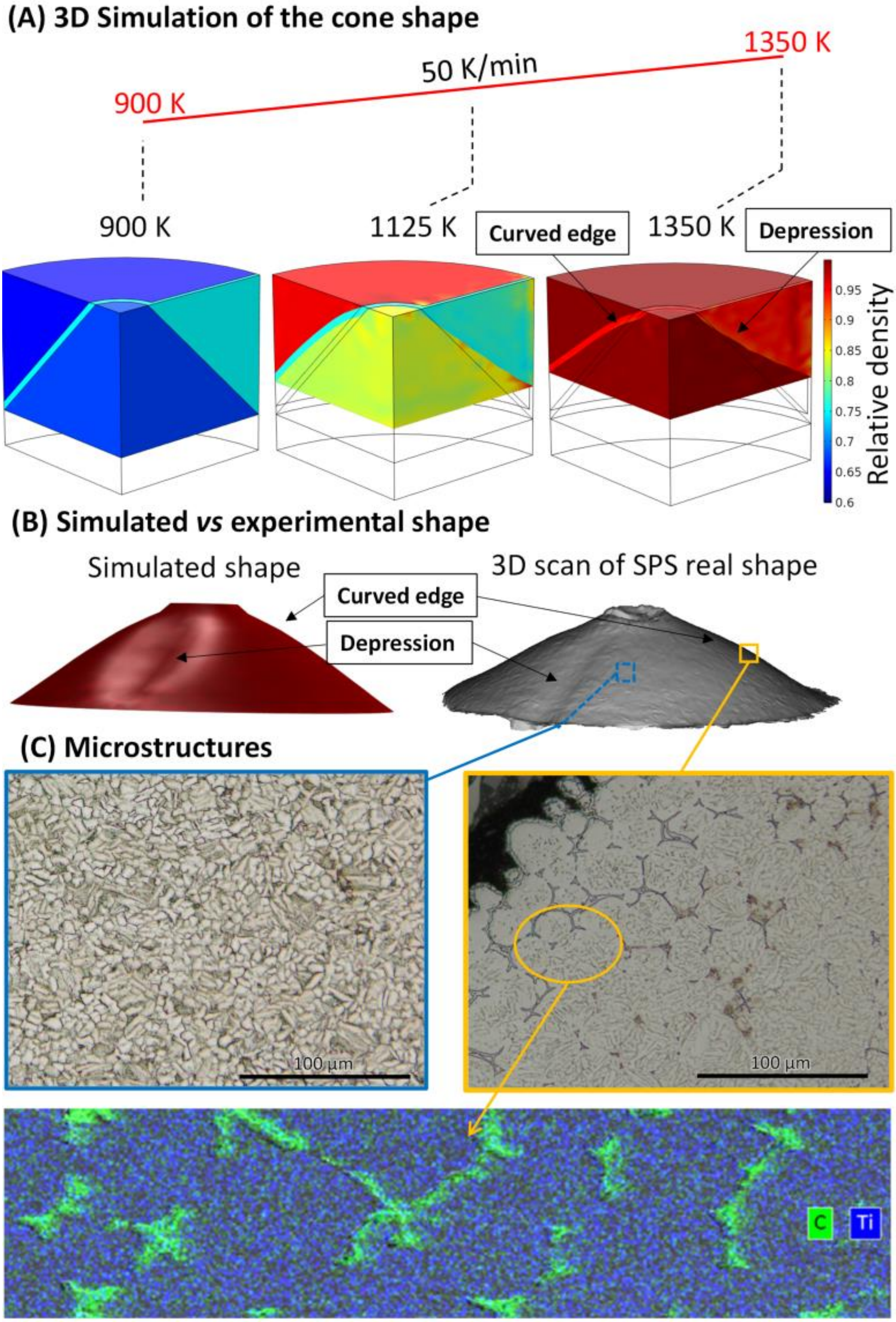

(A) 3D Simulation of the cone shape

(B) Simulated *vs* experimental shape

(C) Microstructures

Figure 6 : (a) Sintering simulation of the cone assembly (b) Final simulated shape and 3D scan of the experimental cone. (c) Microstructures of the experimental cone at two different locations, with, for the edge, an EDSmap showing local carbon rich zones near the interface.

3.4. Turbine blade case

In Figure 7.a, the simulated relative density evolution during the sintering of the turbine blade assembly is reported. The sacrificial powder sinters at slightly lower temperature than Ti-6Al-4V, as expected, but the turbine blade density reaches a high relative density at the end of the dwell. Distortions of the interface structure on the upper surface seems to appear at the end of the dwell. The slice view (in Figure 7.b) gives a better inspection of the turbine blade internal interface. Before reaching the maximum temperature, at 1137 K, the turbine blade is not completely densified and reaches a relative density of 80-85 % while the sacrificial powder reaches a relative density of about 95 %. At the end of the dwell, the whole turbine blade reaches a relative density superior to 95 %. Shape defects also appear on the twist of the turbine blade. The top and the bottom of the twist undergo shrinkage. In a previous article [21], we showed that this defect is due to the slightly higher rigidity of the interface.

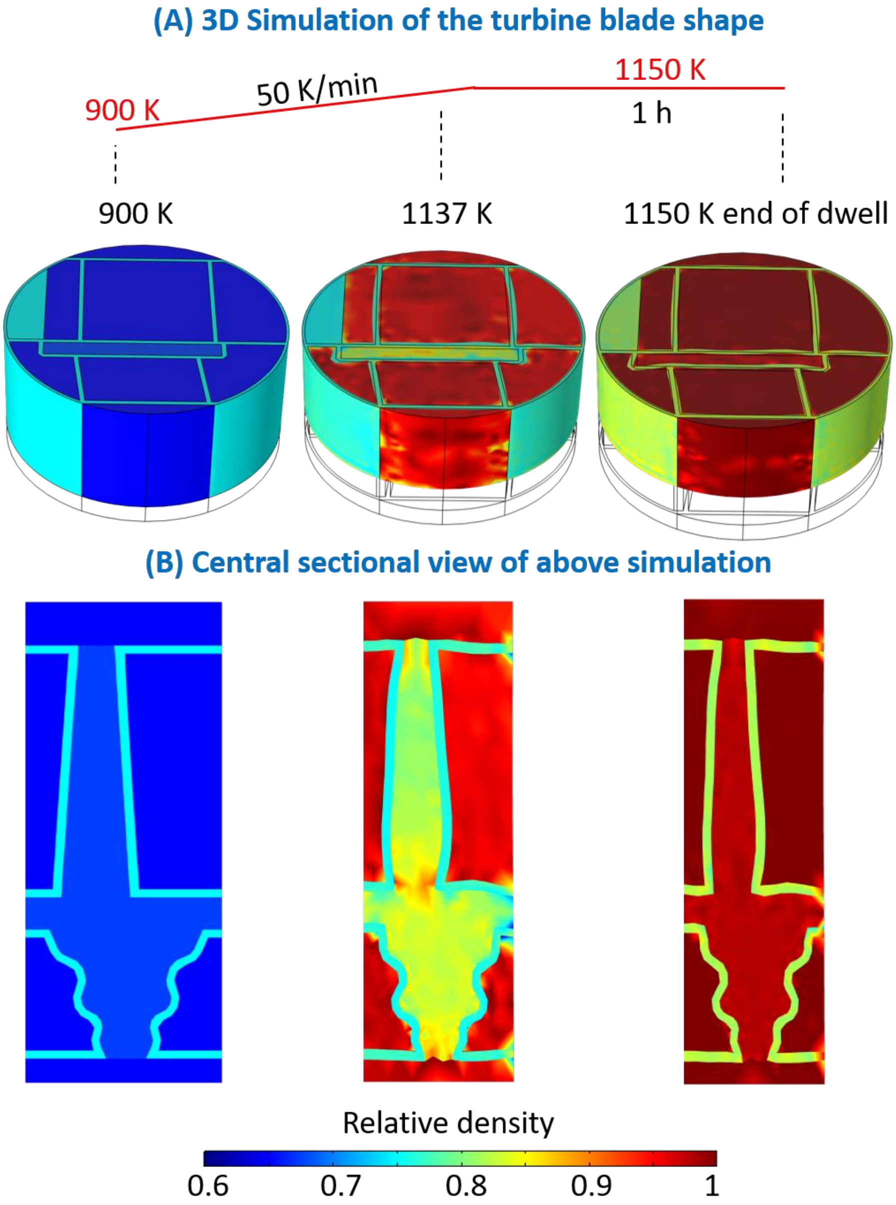

Figure 7 : (a) Evolution of simulated relative density over time of the whole turbine blade assembly. (b) Slice view of the turbine blade assembly during simulated sintering.

In Figure 8, different views of simulated turbine blade and photos of the experimental ones are reported to compare their geometries. In the slice view, the twist shrinkages are noticeable on the experimental and simulated turbine blades. The distortions of the plate are visible on both views of the turbine blades. In the experimental top view, a roughness forming a wood like lines can be seen. Those lines correspond to the 3D printing layers present at the external surface of the interfaces. Still in the top view, the twist is deformed next to a vertical interface wall placed in the sacrificial zone. All of those defects have already been evidenced in a previous work [21] and are not due to the sacrificial powder itself but to the interface which has a different sintering behavior than the part/sacrificial powders. No major shape differences can be detected between the simulated and the experimental turbine blades. Those experiments show that the ceramic-metal powder mix as sacrificial powder allows to follow the sintering of complex shape without exaggerating the shapes distortions originated by the interface.

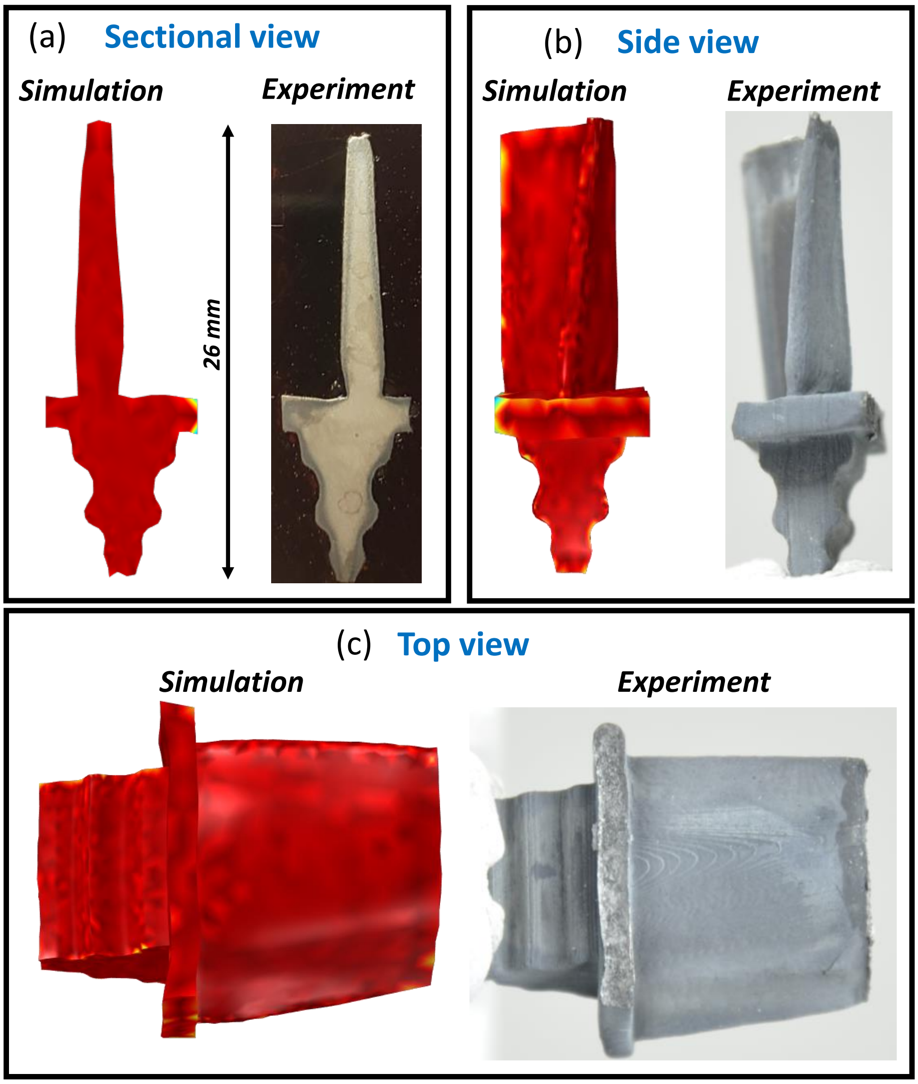

Figure 8: Shape comparison between the simulated and experimentally sintered turbine blade with in (a) the sectional view, (b) the side view and (c) the top view.

In Figure 9, the microstructure study of the turbine blade is reported. Those microstructures reveal a 400 µm thick porosity skin that the simulation does not predict. In the slice of the turbine blade micrograph (Figure 9.a), this skin is noticeable by a darker zone on the edges of the turbine blade. As shown by the micrographs Figure 9.b and c, the darker zone has more porosity than the brighter zone. The micrographs in the core of the turbine blade, Figure 9.d and e, reveal a fully dense or near-fully dense material (brighter zones). It is worthy to note that the porosity zones (like for instance in Figure 9.b) only correspond to the dark “skin” of the photo in Figure 9.a, while the white inner zones, even in the top blade area, are dense like in Figure 9.d. The turbine blade relative density measured by Archimede’s method is 94 % with 1.6 % of open porosity and 4.4 % closed porosity. A previous work [21] has shown that turbine blade edges undergo carbon and other element contamination during sintering. In this article the temperature is higher than the transus. However, this skin phenomenon does not appear if the same alloy is placed in the sacrificial zone. An aqueous slurry is used to ease the preparation of the mixture ceramic-metal sacrificial powder. One possible explanation of this skin phenomenon is that the water desorption increases the pollution penetration in the turbine blade during the debinding stage. Then, the carbon contamination could rigidify and slow the sintering mechanisms in the affected areas. Even if a higher temperature is used in the previous study [21], the presence of the globular phase in the cone case suggests deeper contamination near the edge. The previously used simulation model is purely mechanical and cannot detect chemical interaction affecting the sintering and, consequently, could not predict this porosity skin defect.

The turbine blade’s microstructure consists mainly of coarse α lamellae, with occasional globular α shape resulting from their fragmentation. A turbine blade maximum heating temperature lower than the cone, together with probable contamination, should lead to a large amount of α phase at maximum temperature, and also to a coarsening regime explaining the coarse microstructure.

The hardness measured on the turbine blade is $HV_{0.5}$ 538 ± 15 and is homogeneous all over the section. This hardness is also higher than values reported by the scientific community for Ti-6Al-4V [20, 37, 38]. As mentioned earlier, a possible contamination can also increase the hardness of the turbine blade by solid solution hardening. This higher hardness reinforces the hypothesis of higher and deeper contamination during the debinding due to the aqueous slurry preparation. This skin effect seems to disappear if higher temperatures are applied like in the cone case.

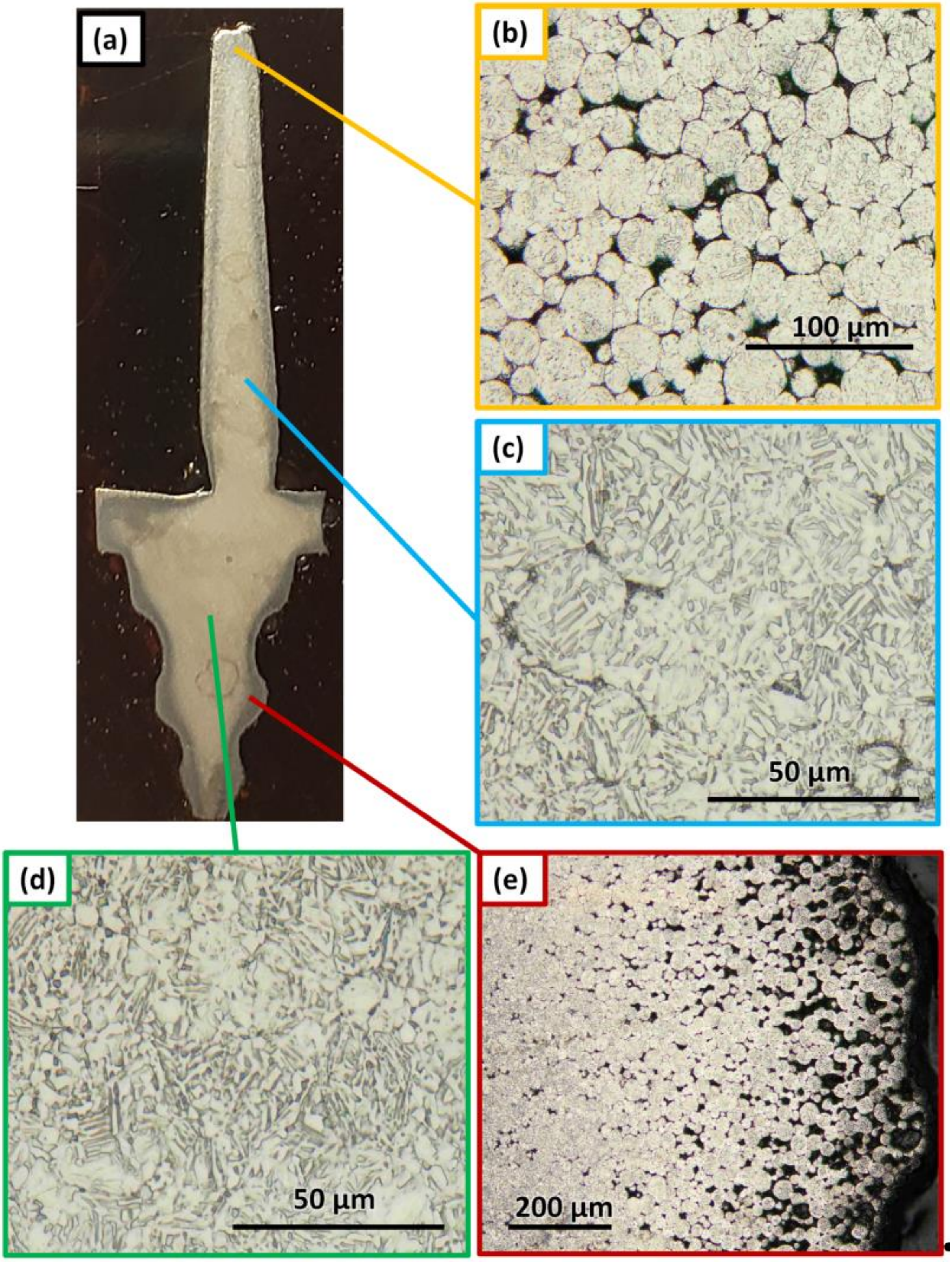

Figure 9: Micrographs of the experimental turbine blade; (a) section, (b) twist skin, (c) twist core, (d) support core, (e) support skin.

The SEM image and EDSmap of the turbine blade skin porous microstructure are shown in Figure 10. The SEM microstructure appears to display a core/shell structure. However, the EDS map does not clearly reveal this core/shell configuration through elemental analysis. Aside from a higher carbon /oxygen concentration at the particle edges, there are no distinct element-rich zones as seen in the cone. This suggests that the pollution penetrates deeply into the grain located near the interface. Similarly, the pollution appears to penetrate further into shapes with thicker skin effects.

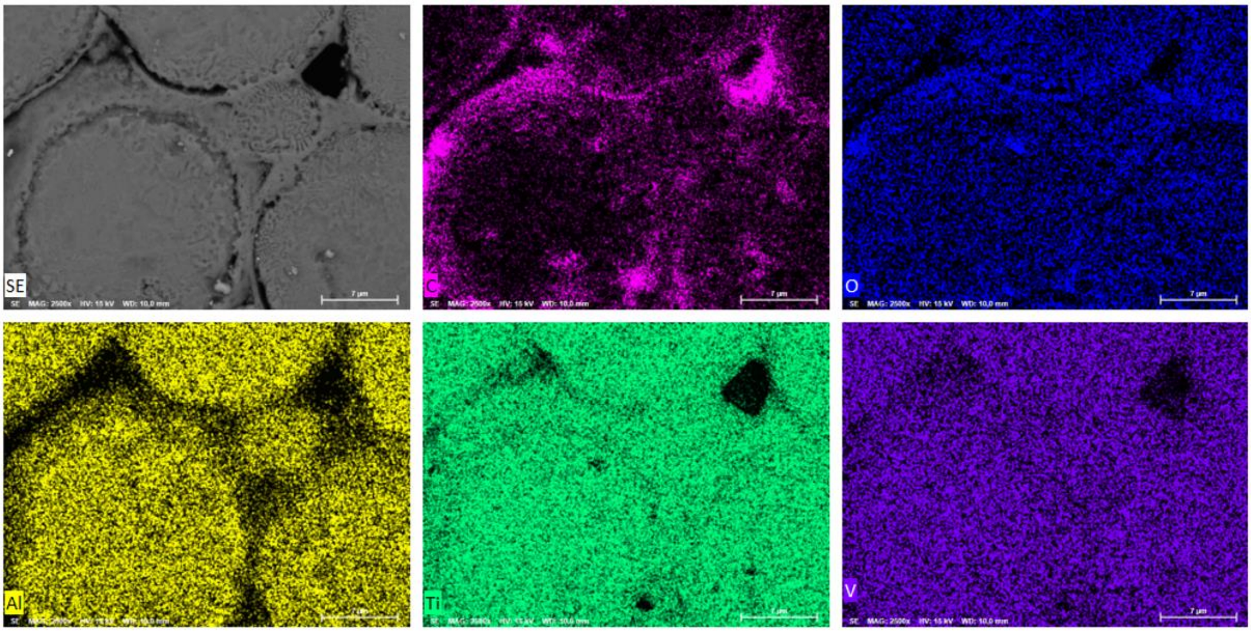

Figure 10 EDSmap of the thick skin microstructure of the turbine blade.

4. Conclusion

In this study, a low-cost ceramic-metal sacrificial powder mixture was tested for fabricating complex Ti-6Al-4V shapes using SPS. This powder mixture mimics the sintering behavior of the Ti-6Al-4V powder, exhibiting a similar shrinkage amplitude and a slightly lower sintering temperature. The sintering behavior of this powder mixture was identified experimentally and validated by analytical methods. The powder mixture has an apparent activation energy of 308 kJ/mol and sintering moduli similar to those of the titanium alloy. Finite element simulations of assemblies comprising three materials (sacrificial, interface, and desired) have been conducted for both a thick cone shape and a thin, highly complex turbine blade shape. The simulation predicts well the main shapes distortions that originate from the interface. The sacrificial powder does not exacerbate shapes defects. However, the small difference in sintering behavior was significant enough to cause the thin turbine blade shape to break. To overcome this problem, a one hour cycle at lower temperature was selected. This cycle reveals a 400 µm skin with higher porosity rate on the turbine blade surface and a higher hardness in its core. This suggests that the aqueous preparation of the sacrificial powder increases the penetration of carbon contamination into the turbine blade during the debinding stage. This phenomenon has not yet been simulated as it is a chemical reaction. However, given that real shapes are likely to be larger than this 30 mm thin blade, the skin effect is expected to be less significant for bigger shapes, assuming they have the same interface thickness.

5. Acknowledgements

The authors thank the Normandy RIN Region Project DEFORMINT n°20191118181931000002100000257 for the financial support of this study. Jérôme LECOURT and Christelle BILOT are thanked for their help on the SPS and microstructure analysis.

References

1. Guillon O, Gonzalez-Julian J, Dargatz B, et al (2014) Field-Assisted Sintering Technology/Spark Plasma Sintering: Mechanisms, Materials, and Technology Developments. Adv Eng Mater 16:830–849. https://doi.org/10.1002/adem.201300409
2. Wei X, Izhvanov O, Back C, et al (2018) Spark plasma sintering of structure-tailored ultrahigh-temperature components: First step to complex net shaping. J Am Ceram Soc 102:1–12. https://doi.org/10.1111/jace.15752

3. Hu Z-Y, Zhang Z-H, Cheng X-W, et al (2020) A review of multi-physical fields induced phenomena and effects in spark plasma sintering: Fundamentals and applications. Mater Des 191:108662. https://doi.org/10.1016/j.matdes.2020.108662

4. Voisin T, Monchoux J-P, Durand L, et al (2015) An Innovative Way to Produce γ-TiAl Blades: Spark Plasma Sintering. Adv Eng Mater 17:1408–1413. https://doi.org/10.1002/adem.201500019

5. German RM (1998) Powder metallurgy of iron and steel. Choice Rev Online 36:36–0981. https://doi.org/10.5860/CHOICE.36-0981

6. Manière C, Durand L, Weibel A, et al (2016) A sacrificial material approach for spark plasma sintering of complex shapes. Scr Mater 124:126–128. https://doi.org/10.1016/j.scriptamat.2016.07.006

7. Manière C, Nigito E, Durand L, et al (2017) Spark plasma sintering and complex shapes: The deformed interfaces approach. Powder Technol 320:340–345. https://doi.org/10.1016/j.powtec.2017.07.048

8. Manière C, Olevsky EA (2018) In situ partially degradable separation interface for fabrication of complex near net shape objects by pressure assited sintering, Patent US 2021/0016499 A1

9. Manière C, Lee G, Olevsky EA (2022) Flash sintering of complex shapes. Appl Mater Today 26:101293. https://doi.org/10.1016/j.apmt.2021.101293

10. Chartier T, Badev A (2013) Rapid Prototyping of Ceramics. In: Handbook of Advanced Ceramics. Elsevier, pp 489–524

11. Halloran JW (2016) Ceramic Stereolithography: Additive Manufacturing for Ceramics by Photopolymerization. Annu Rev Mater Res 46:19–40. https://doi.org/10.1146/annurev-matsci-070115-031841

12. Deckers J, Vleugels J, Kruth JP (2014) Additive Manufacturing of Ceramics: A Review. J Ceram Sci Technol 5:245–260. https://doi.org/10.4416/JCST2014-00032

13. Lakhdar Y, Tuck C, Binner J, et al (2021) Additive manufacturing of advanced ceramic

materials. Prog Mater Sci 116:100736. https://doi.org/10.1016/j.pmatsci.2020.100736

14. Chen Z, Li Z, Li J, et al (2019) 3D printing of ceramics: A review. J Eur Ceram Soc 39:661–687. https://doi.org/10.1016/j.jeurceramsoc.2018.11.013
15. German RM (1996) Sintering Theory and Practice, Wiley. Wiley
16. Hocquet S, Dupont V, Cambier F, et al (2020) Densification of complex shape ceramics parts by SPS. J Eur Ceram Soc 40:2586–2596. https://doi.org/10.1016/j.jeurceramsoc.2019.10.038
17. Zhao Q, Wang H, Tu B, et al (2023) KNbTeO6 transparent ceramics prepared by the combination of pressure-less sintering and pseudo hot isostatic pressing. J Eur Ceram Soc 43:4226–4231. https://doi.org/10.1016/j.jeurceramsoc.2023.03.025
18. Manière C, Durand L, Estournès C (2016) Powder/die friction in the spark plasma sintering process: Modelling and experimental identification. Scr Mater 116:139–142. https://doi.org/10.1016/j.scriptamat.2016.01.040
19. Li C, Liu JF, Guo YB (2016) Prediction of Residual Stress and Part Distortion in Selective Laser Melting. Procedia CIRP 45:171–174. https://doi.org/10.1016/j.procir.2016.02.058
20. Yan Q, Chen B, Kang N, et al (2020) Comparison study on microstructure and mechanical properties of Ti-6Al-4V alloys fabricated by powder-based selective-laser-melting and sintering methods. Mater Charact 164:. https://doi.org/10.1016/j.matchar.2020.110358
21. Le Cloarec J, Marinel S, Estournès C, et al (2024) Stereolithography coupled with spark plasma sintering to produce Ti-6Al-4V complex shapes. J Manuf Process 114:122–135. https://doi.org/10.1016/j.jmapro.2024.01.084
22. Li W, Olevsky EA, McKittrick J, et al (2012) Densification mechanisms of spark plasma sintering: multi-step pressure dilatometry. J Mater Sci 47:7036–7046. https://doi.org/10.1007/s10853-012-6515-y
23. Manière C, Durand L, Weibel A, Estournès C (2016) Spark-plasma-sintering and finite

element method: From the identification of the sintering parameters of a submicronic α -alumina powder to the development of complex shapes. Acta Mater 102:169–175. https://doi.org/10.1016/j.actamat.2015.09.003

24. Manière C, Durand L, Chevallier G, Estournès C (2018) A spark plasma sintering densification modeling approach: from polymer, metals to ceramics. J Mater Sci 53:7869–7876. https://doi.org/10.1007/s10853-018-2096-8

25. Grippi T, Torresani E, Maximenko AL, Olevsky EA (2024) Additive manufacturing-assisted sintering: Low pressure, low temperature spark plasma sintering of tungsten carbide complex shapes. Ceram Int 50:37228–37240. https://doi.org/10.1016/j.ceramint.2024.03.311

26. Torresani E, Carrillo M, Haines C, et al (2023) Fabrication of powder components with internal channels by spark plasma sintering and additive manufacturing. J Eur Ceram Soc 43:1117–1126. https://doi.org/10.1016/j.jeurceramsoc.2022.11.008

27. Olevsky EA (1998) Theory of sintering: from discrete to continuum. Mater Sci Eng R Reports 23:41–100. https://doi.org/10.1016/S0927-796X(98)00009-6

28. Manière C, Harnois C, Marinel S (2021) Porous stage assessment of pressure assisted sintering modeling parameters: a ceramic identification method insensitive to final stage grain growth disturbance. Acta Mater 211:116899. https://doi.org/10.1016/j.actamat.2021.116899

29. Manière C, Diatta JS, Harnois C, et al (2023) Pressure assisted sintering stress exponent assessment methods: Accuracy analysis and effect of sintering stress. Mech Mater 181:104664. https://doi.org/10.1016/j.mechmat.2023.104664

30. Diatta JS, Couder C, Harnois C, et al (2023) Modeling spark plasma sintering of zirconia with prediction of final stage high densification rate. Mater Lett 337:133930. https://doi.org/10.1016/j.matlet.2023.133930

31. Manière C, Grippi T, Marinel S (2022) Estimate microstructure development from sintering shrinkage: A kinetic field approach. Mater Today Commun 31:103269.

https://doi.org/10.1016/j.mtcomm.2022.103269

32. Rahaman MN (2007) Sintering of Ceramics, CRC Press

33. Langer J, Hoffmann MJ, Guillon O (2009) Direct comparison between hot pressing and electric field-assisted sintering of submicron alumina. Acta Mater 57:5454–5465. https://doi.org/10.1016/j.actamat.2009.07.043

34. Manière C, Diatta JS, Couder C, et al (2023) Spark plasma sintering grain growth assessment by densification kinetics analysis. Scr Mater 228:115346. https://doi.org/10.1016/j.scriptamat.2023.115346

35. Weiss I, Froes FH, Eylon D, Welsch GE (1986) Modification of alpha morphology in Ti-6Al-4V by thermomechanical processing. Metall Trans A 17:1935–1947. https://doi.org/10.1007/BF02644991

36. Dong E, Yu W, Cai Q (2017) Alpha-case kinetics and high temperature plasticity of Ti-6Al-4V alloy oxidized in different phase regions. Procedia Eng 207:2149–2154. https://doi.org/10.1016/j.proeng.2017.10.973

37. Ayodele OO, Awotunde MA, Shongwe MB, et al (2019) Densification and microstructures of hybrid sintering of titanium alloy. Mater Today Proc 28:781–784. https://doi.org/10.1016/j.matpr.2019.12.297

38. Singh N, Ummethala R, Karamched PS, et al (2021) Spark plasma sintering of Ti6Al4V metal matrix composites: Microstructure, mechanical and corrosion properties. J Alloys Compd 865:158875. https://doi.org/10.1016/j.jallcom.2021.158875